Tailoring hierarchical microstructures and nanoprecipitates in additive-manufactured Al-Zn-Mg-Cu-Nb alloys for simultaneously enhancing strength and ductility

Check for updates

Fei Xiao[1], Da Shu [1 ✉], Yixiao Wang[2], Qinyao Sun[1], Donghong Wang[1], Chao Yang[1], Shubin Wang[1], Jiawei Mi [3] & Baode Sun[1 ✉] & David H. StJohn [4]

Additive manufacturing provides an efficient way of producing metallic components with complex geometries. Their microstructure is substantially different to those from conventional processing, creating opportunities for manipulating the final microstructure and properties via heat treatment. Here, we demonstrate that as-built heterostructures in an Al-Zn-Mg-Cu-Nb alloy produced during the solidification of molten pools provide a driving force and additional Zener pinning sources for recrystallization. This creates a bimodal grain structure after solution treatment, causing additional hetero-deformation-induced strengthening and hardening. Coarse grains are found to promote work hardening and blunt the propagate of cracks during deformation, increasing ductility. Together with precipitation strengthening from a high number density nanoprecipitates, the simultaneous improvement of strength and ductility in a highly alloyed Al-Zn-Mg-Cu-Nb alloy is achieved. These results provide a simple strategy for the development of additively manufactured age-hardening alloys with improved strength and ductility for high performance structural applications.

Conventional processing of alloys, usually comprising melting, casting, homogenization, multiple deformation steps and heat treatment, has high cost, low efficiency, high energy consumption and significant CO_2 emissions. Laser powder bed fusion (LPBF) is one of the widely used additive manufacturing (AM) technologies, in which an intensive laser beam is used to melt and fuse the added powder feedstock layer by layer to build a complex-shaped 3D object with little material loss[1]. A wide range of metallic alloy powders are often used as the feedstock materials in LPBF, including aluminum, titanium, nickel based high strength alloys and a certain type of steels.

However, most of the commercial alloys with high strength have higher weight percentage of solutes with large solidification temperature range,

making them to be susceptible to hot tearing or crack in LPBF process[2,3]. Effective grain refinement by in-situ formation of primary phases or direct addition of heterogeneous nucleant particles (TiB$_2$, TiC, etc.) has been shown as an effective way to inhibit hot cracks[3–5]. Taking high-strength aluminum alloys as an example, it is difficult to obtain a wide process window for crack-free components only by adjusting LPBF parameters, leading to poor formability and deteriorated mechanical properties[3,6,7]. Some ceramic particles are added to aluminum alloy powders as external nucleation sites to refine grain size and suppress hot cracking. For example, Zhou et al. [8] eliminated hot cracks of 7075 aluminum alloy by adding submicron Si and TiB$_2$ particles at the same time owing to narrowing the solidification interval and improving the fluidity, and the tensile strength of

[1]Shanghai Key Lab of Advanced High-temperature Materials and Precision Forming and State Key Lab of Metal Matrix Composites, School of Materials Science and Engineering, Shanghai Jiao Tong University, Shanghai 200240, China. [2]National Engineering Research Center of Light Alloy Net Forming and State Key Laboratory of Metal Matrix Composites, School of Materials Science and Engineering, Shanghai Jiao Tong University, Shanghai 200240, China. [3]School of Engineering, University of Hull, Hull HU6 7RX, UK. [4]School of Mechanical and Mining Engineering, University of Queensland; St. Lucia, Brisbane, QLD 4072, Australia. ✉e-mail: dshu@sjtu.edu.cn; bdsun@sjtu.edu.cn

T6 treated alloy was ~500 MPa, but the elongation was <5%. Recently, elements such as Sc, Zr, and Ti have been added to aluminum alloy powders to generate primary nucleation sites, resulting in high-strength aluminum alloys without cracks. For example, the 1.5wt.%Ti-modified Al-Cu-Mg alloy possesses high ultimate tensile strength of ~426 MPa, yield strength of ~293 MPa and elongation to failure of ~9 %, which is significantly higher than the mechanical properties of unmodified alloys due to the elimination of hot cracks[9]. Zhu et al.[5] reported that the yield strength and elongation of the LPBFed Al-6.78Zn-2.53Mg-1.94Cu-0.46Sc-0.23Zr alloy are ~647 MPa and ~11.6% respectively after T6 treatment, which can be attributed to the strengthening effect caused by η′/Al$_3$(Sc, Zr) nanoprecipitates and other multi-scale precipitates. Based on these studies, eliminating hot cracks while generating high-density nanoprecipitates is an effective way to prepare AMed high-strength aluminum alloys. Nevertheless, it is undoubted that there are upper limits on the content of strengthening elements in various precipitation hardening alloys, and excessively high levels of alloying elements can damage the formability of LPBF[10–12]. Therefore, it is necessary to search for additional strengthening methods for fabricating LPBFed alloys with super strength, high ductility and low cost.

Interestingly, special thermal history and the extreme metallurgical conditions during LPBF lead to distribution differences of primary phases and additional heterogeneous nucleation sites in molten pools, which will increase the heterogeneity of grain size and residual strain[13–15]. Post heat treatment, including solution and aging, is a common method to improve the mechanical properties of heat-treated alloys. If the solution temperature is higher than the recrystallization temperature, recrystallization will occur, which usually reduces the strength and improves the ductility[16,17]. Due to the extremely fast cooling rate ($10^3 \sim 10^8$ K/s) during LPBF, a large number of dislocations and residual stresses are generated, which provides a driving force for recrystallization[18,19]. In the LPBF process of alloys containing primary phases and additional nucleating particles, the grains are significantly refined, resulting in a large number of high-energy grain boundaries that facilitate recrystallization[20,21]. Therefore, the heterogeneous microstructures produced by LPBF will have a different response to a particular heat treatment compared to that of a conventionally-manufactured part, which will generate hierarchical microstructures with the potential to further enhance mechanical performance after post heat treatment.

In this work, we design a highly alloyed Al-Zn-Mg-Cu-Nb alloy that is tailored for LPBF and introduce bimodal grains that can be tuned by post solution heat treatment to achieve the simultaneous improvement of strength and ductility. To overcome the typical strength-ductility dilemma in AM produced age-hardening Al alloys, the following strategy has been adopted: (1) increasing the content of the main precipitate forming elements, Zn and Mg, in the pre-alloyed powders ensuring a high number density of η′ (MgZn$_2$) precipitates in the final state; (2) adding Nb nanoparticles to the powders to promote grain refinement during LPBF for crack inhibition; (3) implementing a post solution treatment to obtain a bimodal grain structure by tailoring the volume of the recrystallized grains; and finally (4) imposing a peak aging heat treatment to achieve the complete precipitation of η′ nanoprecipitates.

Results
The mechanical properties of the heat-treated alloys with bimodal grains and nanoprecipitates

After LPBF of the Nb nanoparticle-modified Al-Zn-Mg-Cu powders, a crack-free and fully equiaxed microstructure is obtained with ultrafine grains (UFGs) and fine grains (FGs) alternately distributed in each solidified molten pool, as shown in Fig. 1a, which can be attributed to the strong nucleation ability of the Al$_3$Nb primary phase[22]. From Fig. 1a, the volume faction of the UFGs in the as-built alloy is ~70%, while the volume faction of the FGs is ~30%. However, a bimodal grain structure formed after 450℃/20 min solution, as shown in Fig. 1b, consists of alternating zones of coarse grains (CGs) and fine grains (FGs), in which the volume fraction of the FGs is ~18%. The proportion of CGs increases with the increase of solution temperature and time (see Supplementary Fig. 1), indicating that the

bimodal structure can be controlled by adjusting solution treatment parameters. Upon a further peak aging treatment (120℃/24 h), η′ nanoprecipitates having an average size of ~5 nm and an approximately equal number density are observed in both CGs and FGs zones, as shown in Fig. 1c-h. Supplementary Figs. 2–4 show that the change of solid solution parameters has no significant effect on the size and volume fraction of the η′ nanoprecipitates and the peak-aging time. At 450℃, the η′ phase in the as-built alloy can be completely dissolved within 3 min (see Supplementary Note 1 and Supplementary Fig. 6), which implies that sufficient Zn/Mg solutes can be used for the subsequent aging even after short-time solid solution at relatively low temperature. Therefore, the contribution of precipitation strengthening to yield strength is similar in peak aged alloys after different solid solution treatments.

The tensile engineering stress-strain curves and a summary of the tensile properties for LPBF samples after various solution treatments and peak aging are given in Figs. 2a and 2b, respectively. The yield plateau and Lüders band appear in the tensile curves of the as-built sample, which is caused by dynamic strain aging due to the dynamic interaction between movable dislocations and solute atoms[23,24]. The sample after 450℃/20 min solution and peak aging treatments displays superior strength and good ductility, with an ultimate tensile strength (UTS) and a yield strength (YS) as high as 728 MPa and 648 MPa respectively, and an elongation (EL) of ~5.1%. In contrast, a significant reduction in the strength is observed for the sample after 490℃/60 min solution and peak aging, in which the FGs and bimodal grain microstructure almost disappear, although EL increases to ~6.6%. Furthermore, the strain hardening rate, also known as work hardening rate ($\theta = d\sigma/d\varepsilon$, where σ is the true stress and ε is the true strain), of the sample solution-treated at 450℃/20 min is improved (Fig. 2c). Therefore, it produced the highest UTS among the various LPBF-processed Al alloys, including Sc-containing aluminum alloys (Fig. 2e).

The contributions from grain boundary strengthening (σ_{GB}), precipitation strengthening (σ_P), solid solution strengthening (σ_{SS}), and dispersion strengthening (σ_{DIS}) are estimated in the Supplementary Note 2. Figure 2d shows that precipitation strengthening is the main reason for the high strength in the alloys, which can be attributed to the high number density η′ nanoprecipitates. Supplementary Table 4 represents the difference between the calculated values and experimental values of yield strength. Except for the sample treated by 490℃/60 min and peak aging, the calculated strength values of all other samples are lower than the experimental values. It is inferred that the difference between the calculated strength and the experimental strength should be come from Hetero-Deformation Induced (HDI) strengthening caused by the bimodal grains[25,26].

The relationship between the bimodal grains and melt pools during solid solution

Interestingly, the shape of the FGs zone in Fig. 1b is arc-shaped, which is similar to the shape of the molten pool in Fig. 1a, indicating that they are inherited from those in the as-built sample. We conducted a quasi-in-situ electron backscatter diffraction (EBSD) characterization of the as-built sample prior to and after solution treatment at 450℃/20 min (see Method). As shown in Supplementary Fig. 7, the FGs at the bottom of the solidified molten pool is retained after the solution treatment, while the UFGs at the top of the solidified molten pool grows significantly, resulting in the bimodal grain structure. Moreover, the FGs still maintain the original high angle grain boundaries (HAGBs, >15°) and low angle grain boundaries (LAGBs, 2° ~ 15°), while the LAGBs in CGs are significantly reduced, suggesting that the CGs are formed by recrystallization, which is further confirmed by the release of residual strain in the CGs zones indicated by the kernel average misorientation (KAM) maps.

Heterostructures of the as-built alloy

As the microstructure of the solidified molten pool is the precursor to the formation of bimodal microstructure after solution treatment, we examined
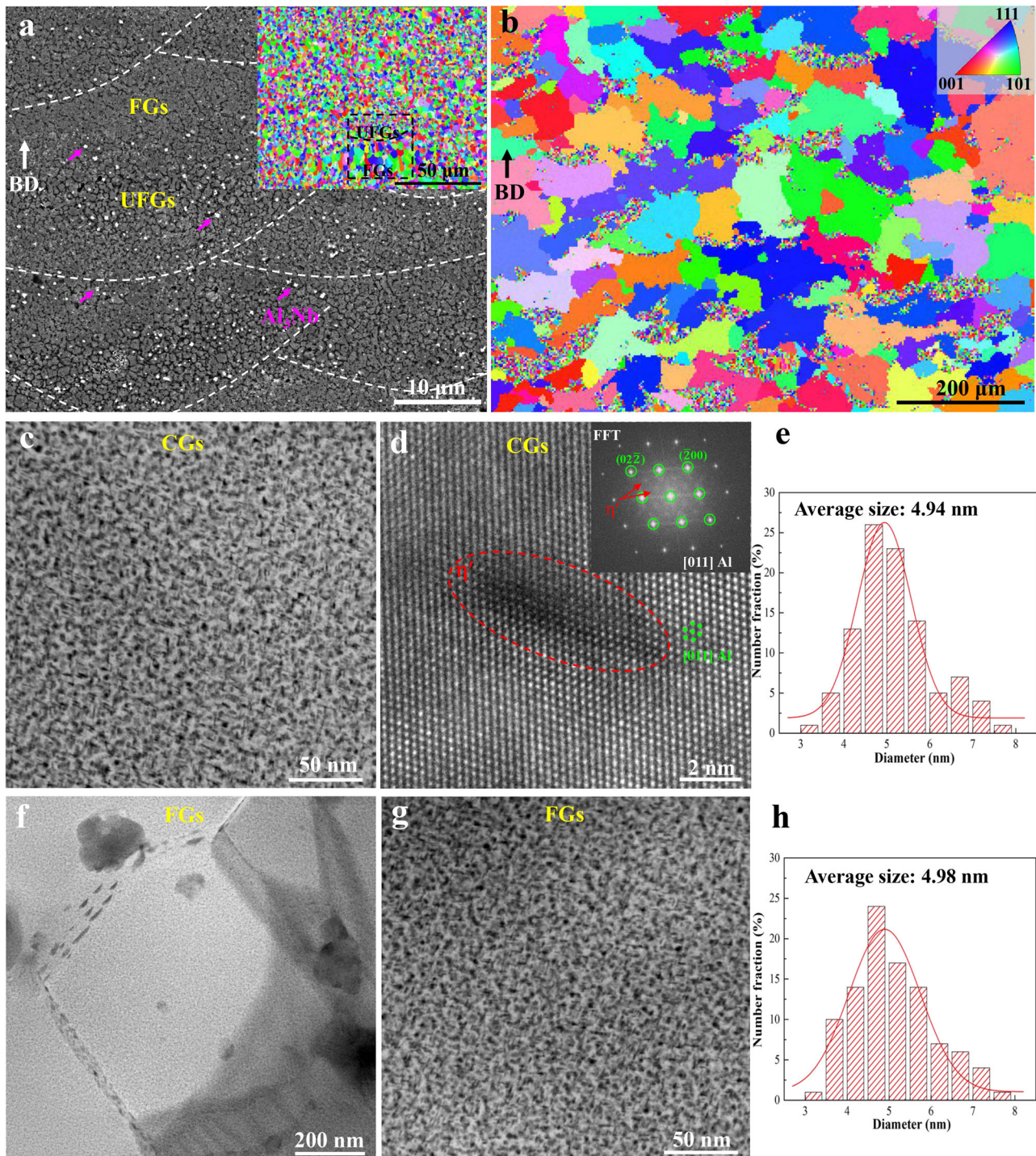
Fig. 1 | Microstructures of the LPBF samples prior to and after solution and peak aging treatment. a A fully equiaxed LPBF microstructure with ultrafine grains (UFGs) and fine grains (FGs) produced by Nb nanoparticles modified Al-Zn-Mg-Cu powders in each molten pool (BD represents the build direction). **b** Bimodal grain structure after 450°C/20 min solution treatment. **c** Nanoprecipitates in a CG after 450°C/20 min solution and peak aging. **d** High-resolution transmission electron microscope (HRTEM) and Fast Fourier Transform (FFT) of η′ in the CG. **f, g** Nanoprecipitates in a FG after 450°C/20 min solution and peak aging. **e, h** Size distribution of nanoprecipitates in the CG and FG, respectively.

the primary phase, grains, dislocations and element distribution in the as-built sample. Due to the enormous surface energy and extremely small volume of nanoparticles, Nb nanoparticles on the surface of aluminum powders can melt within a few microseconds under the action of high-energy lasers[27], and then Al_3Nb were formed as a primary phase from the molten pool, acting as nucleants for aluminum during solidification. A high number of primary Al_3Nb particles are observed in the UFGs zone (Fig. 3a)

while few primary Al_3Nb particles appear in the FGs zone (Fig. 3b). Energy-dispersive spectroscopy (EDS) mapping shows that Nb is enriched in Al_3Nb in the UFGs region but dissolved in Al matrix in the FGs region, owing to the faster cooling rate in the center than at the bottom of the solidified molten pool. This inhomogeneous distribution of the primary Al_3Nb particles (appearing white in the scanning electron microscope (SEM) image) can also be observed in Fig. 1a, which is believed to be caused by different cooling
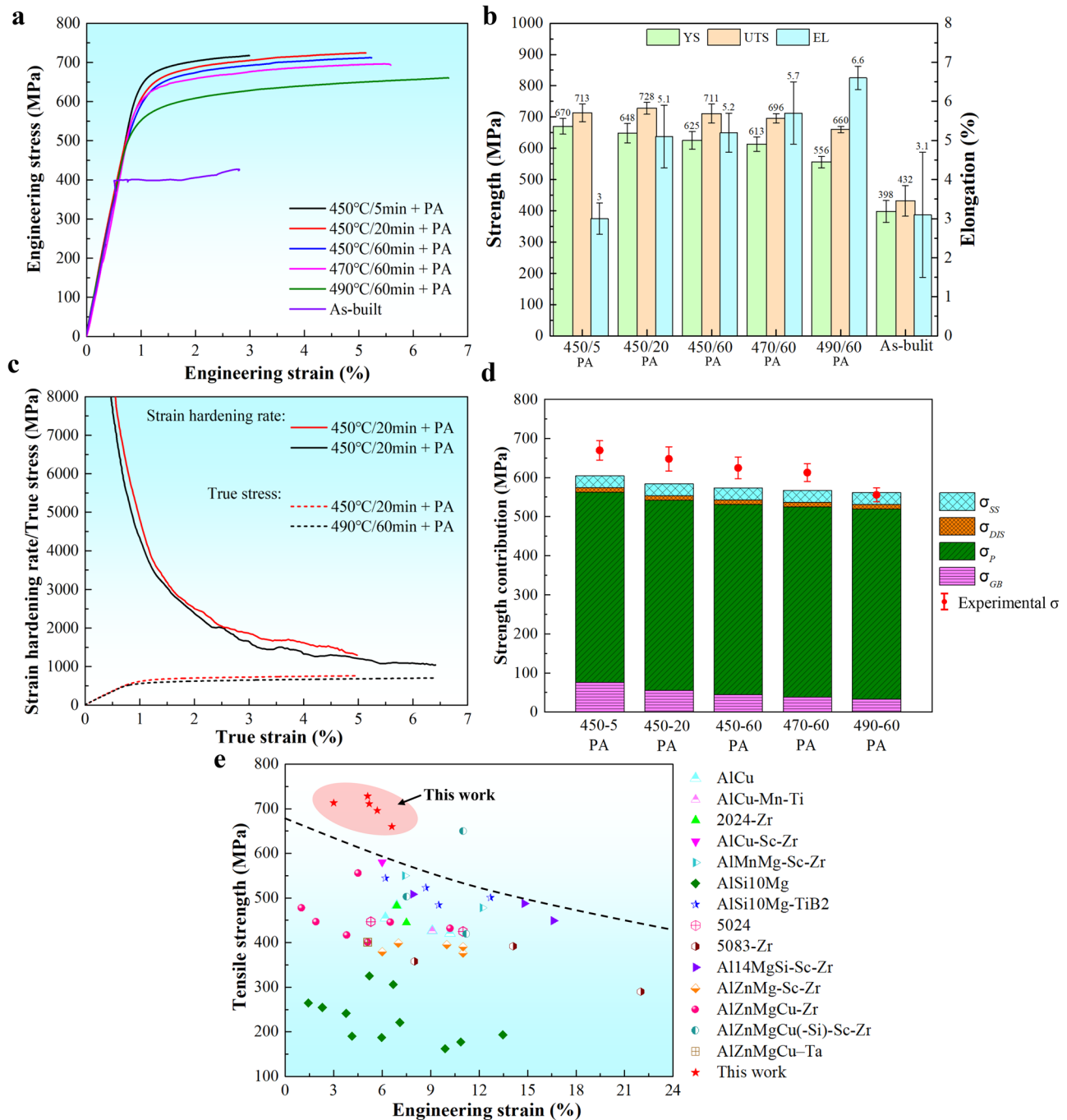
Fig. 2 | Tensile properties of the alloys. a Tensile engineering stress-strain curves for LPBF samples after various solution treatments and peak aging (PA). **b** Summary of tensile properties. **c** Strain-hardening rate curves. **d** Strength contribution from different mechanisms in alloys treated by different heat treatments. **e** Comparison of UTS and elongation to fracture for various LPBF-processed Al alloys. The reference materials include LPBF-processed AlCu-(Mn)-(Ti)-(Zr)[9,56–59], AlMnMgScZr[30,60,61], AlSi10Mg/AlSi10Mg-TiB$_2$ composites[62–65], 5024[66], 5083-Zr[67], AlMgSiScZr[68,69], AlZnMg-Sc-Zr[70], AlZnMgCu-(Si)-(Sc)-(Zr)[3,8,12,71–75], and AlZnMgCu-Ta[76].

rates generated by the complicated solidification history during LPBF[28–30]. In our previous work, kinetic analysis demonstrated that decreasing the cooling rate of the molten pool was beneficial to the formation of Al$_3$Nb[22], which is also confirmed in related research[28]. We have calculated that the critical cooling rate required for the precipitation of the Al$_3$Nb primary phase in Al melt is ~8.08×10^6 K/s[22], as shown in Fig. 3c. When the cooling rate is lower than the critical cooling rate, the Al$_3$Nb primary phase will be formed. Otherwise, the Nb element dissolves into the Al matrix. Therefore, heterostructures were formed in the molten pool. It is worth noting that the distribution of UFGs and FGs in the solidified molten pool is consistent with that of primary Al$_3$Nb particles, demonstrating the excellent nucleating

ability of Al$_3$Nb on Al grains[22]. Due to the thermal mismatch, stress concentration and high-density entangled dislocations are easily generated near the interface between the cubic Al$_3$Nb particles and Al matrix, which is true for the UFGs zone (Fig. 3a).

The recrystallization of UFGs zones to form CGs zones can be understood because of the high driving force provided by the energy stored in the high-density grain boundaries and dislocations around the Al$_3$Nb particles. On the one hand, the difference in the coefficient of thermal expansion between the Al$_3$Nb particles and Al matrix enabled the formation of a deformation zone around Al$_3$Nb particles, which in turn promoted recrystallization[31,32]. At the bottom of the melt
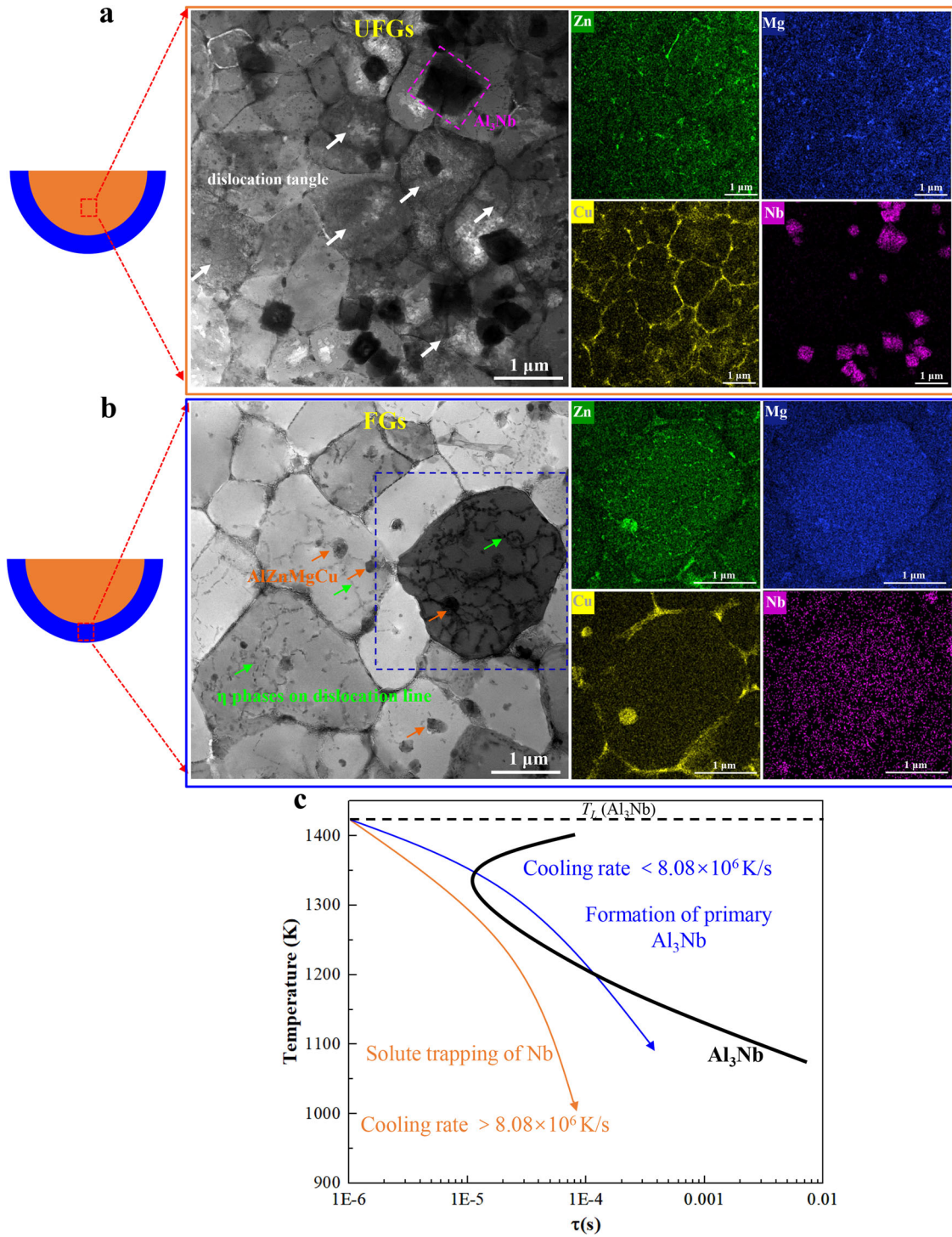
Fig. 3 | Distribution of Al₃Nb primary phase and Nb element in the as-built sample. a TEM-bright field image and corresponding EDS mapping of the UFGs zone. **b** TEM-BF image and corresponding EDS mapping of the blue dashed box in the FGs zone. **c** Calculated incubation time for the competing Al₃Nb primary phase and α-Al, with two cooling curves representative for the center (orange curve) and the bottom (bule curve) of melt pools.

pool, a large number of entangled dislocations are distributed around the Al₃Nb primary phase (Fig. 3a), and the residual strain in the FGs region is larger than that at the top of the melt pool (Supplementary Fig. 7), indicating the presence of significant distortion zone around Al₃Nb, which provides a substantial driving force for recrystallization and grain growth. On the other hand, Al₃Nb can effectively refine α-Al, resulting in a significant increase in grain boundary density. A large amount of enthalpy stored in the high-density grain boundaries promotes recrystallization[20,21].

Heterogeneous distribution of secondary phases during solid solution
Besides the lower driving force for recrystallization, the precipitation of secondary phases, mainly S (Al₂CuMgNb) and Al₇Cu₂Fe, are also responsible for the retention of FGs during the solution treatment. These phases are observed at grain boundaries of FGs after solution at 480 °C/60 min (Fig. 4a), and the corresponding EDS mapping shows the enrichment of Cu, Mg, Nb and Fe elements. TEM-EDS shows that the atomic ratio of (Cu+Nb) to Mg is ~1 (Fig. 4b), indicating Nb atoms dissolved in the FGs
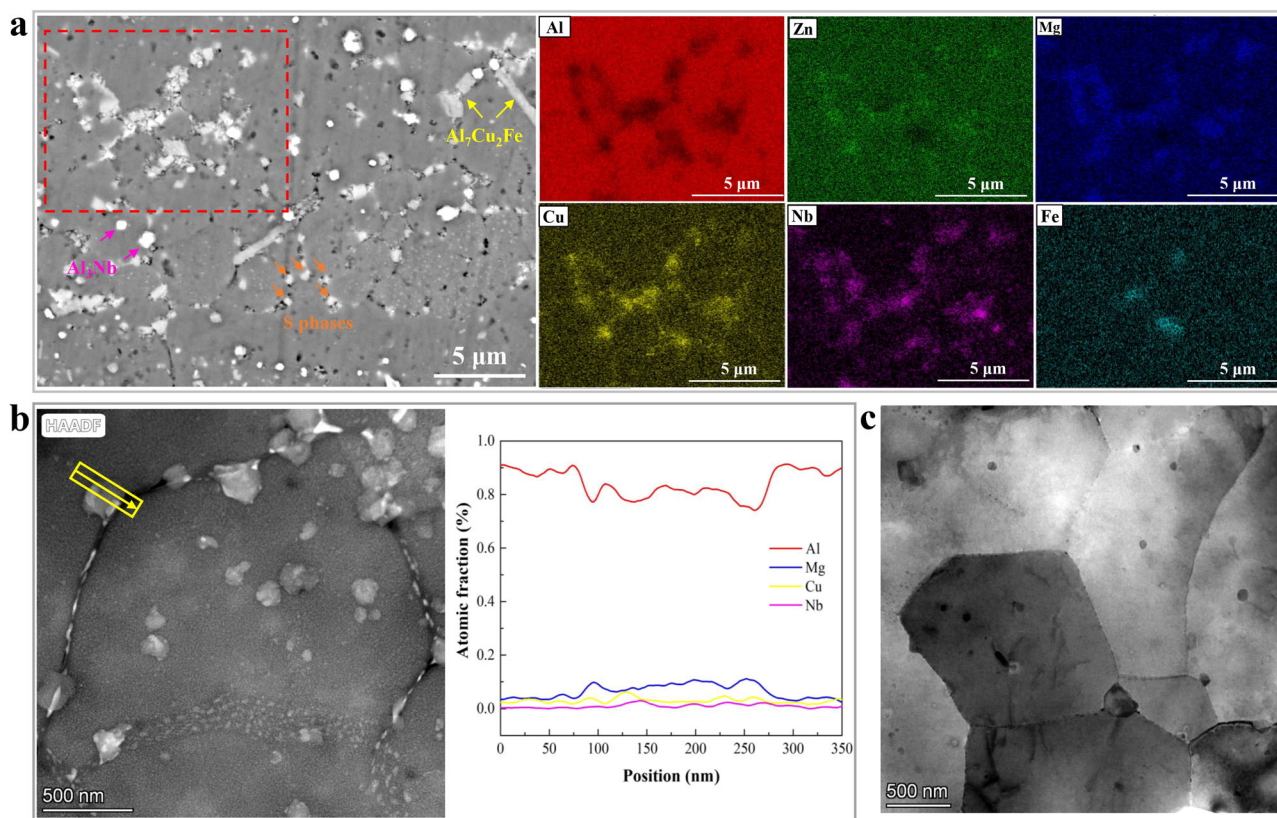
Fig. 4 | Secondary phases in the FGs zone after solution treatment. a SEM image of secondary phases after solution at 480°C/60 min and corresponding EDS maps in the red dashed box. **b** High-angle annular dark field image EDS mapping of the S phase at the grain boundaries. **c** The S phases partially dissolved in the Al matrix after solution at 490°C/60 min.

precipitate and replace some Cu atoms in the S phase during solution treatment. Based on thermodynamic calculations (Supplementary Fig. 8a) and differential scanning calorimetry (DSC) results (Supplementary Fig. 8b), the η phase begins to dissolve at temperatures higher than 440 °C and the S phase begins to dissolve around 480 °C while the Al_7Cu_2Fe phase dissolves above 500 °C. Because the diffusion rate ($\sim 5 \times 10^{-21}$ m^2 s^{-1} at 500° C) of Nb in aluminum is very slow[33], the solid solution of Nb in the S phase can increase its stability during solution. Thus, we can conclude that the retention of FGs benefits significantly from the strong Zener pinning force[34–36] generated by the $Al_2CuMgNb$ phase and the Al_7Cu_2Fe phase at the grain boundaries, which act as obstacles to recrystallization. In contrast, the recrystallization of FGs in the sample after 490°C/60 min solution treatment occurred (Supplementary Fig. 1) because the secondary phases were partially dissolved in the Al matrix at 490°C (Fig. 4c).

In summary, the formation of bimodal grains is closely related to the addition of Nb and the special solidification thermal history of LPBF process. And a schematic diagram of the role of Al_3Nb primary phase and Nb element on the microstructure evolution in molten pool during different solid solution treatments is presented in Supplementary Fig. 9.

Discussion

Common strategies to strengthen alloys include solid solution hardening[37], dislocation hardening[38], grain boundary strengthening[5], precipitation hardening[23], dispersion hardening, and so on. The main strengthening mechanism in this alloy is undoubtedly precipitation strengthening. The bimodal grain structure produced by special solidification thermal history of molten pools, however, provides an additional strengthening mechanism in the additive manufactured alloys: hetero-deformation induced (HDI) strengthening and HDI work hardening[39] (Fig. 2d). Supplementary Fig. 10 shows that the fluctuating microhardness values appear in the sample treated by 450°C/20 min solution and peak aging, where larger average

microhardness values (~228 HV) correspond to the FGs zone, are mainly attributed to smaller grain sizes and the dispersed secondary phases, while smaller hardness values (~186 HV) represent the CGs zone. These zones with different mechanical properties are mechanically incompatible at the elastic-plastic deformation stage and plastic deformation stage, leading to strain partitioning during deformation, where the softer zones usually sustain higher plastic strain[35,40]. As shown in Fig. 5a, obvious dislocation tangles appear in both the CGs and FGs zones after tensile deformation, and particularly the dislocation density and degree of entanglement in the CGs zones are higher, indicating larger plastic deformation in CGs zones.

The inhomogeneity of plastic deformation of the CGs and FGs zones is closely related to strain strengthening and dislocation movement[41]. The soft zone (CGs) has strong dislocation storage capacity and tends to preferentially deform plastically, while the hard zone (FGs) is still under elastic deformation. In order to adapt to the inhomogeneity of plastic deformation, the strain gradient tends to be generated at the interface of soft and hard regions[20,42]. Pileups of geometrically necessary dislocations (GNDs)[20,42,43] are thus generated to accommodate the strain gradient. As a larger KAM value corresponds to a larger GNDs density (ρ_{GND})[44,45], the plastic strain near the interface between FGs and CGs (marked by pink arrows) is significantly higher than that inside the CGs (Fig. 5b). The ρ_{GND} ($\rho_{GND} = \frac{2\theta}{ub}$, where θ represents the local misorientation angle, u is the EBSD step size (250 nm) and b is the Burgers vector of Al (0.286 nm)) along the red arrow direction at the interface between FGs and CGs is shown in Supplementary Fig. 11, which is higher than that of pure Al and aluminum matrix composites with heterostructures[46,47], further indicating the pileups of GNDs at the interface. Pileups of GNDs produce a back stress in the soft zone[48,49] while the front stress is developed in the hard region[49,50]. The interaction between back stress and front stress produces HDI stress during plastic deformation[49,50], which contributes to the improvement of yield strength. In order to confirm the contribution of HDI stress, we carried out loading-unloading-reloading experiments, as shown in Figs. 5d and 5e.
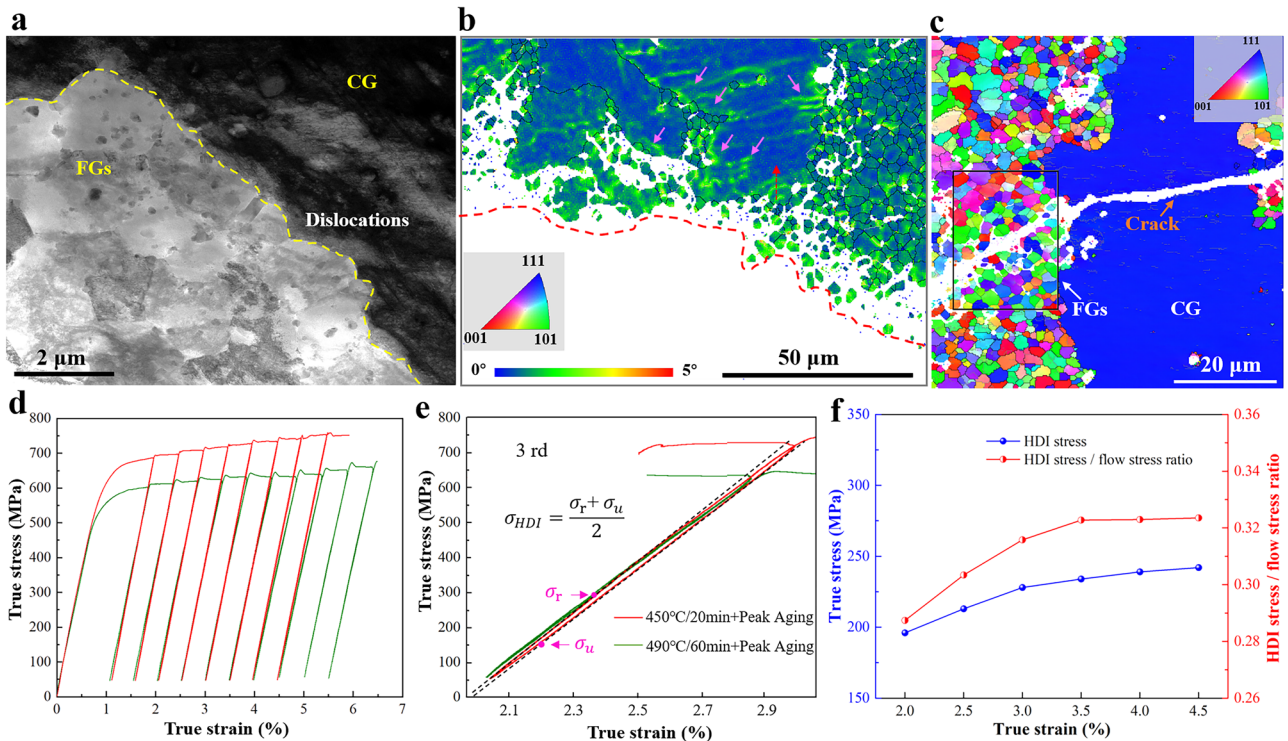
Fig. 5 | Hetero-deformation structure and hetero-deformation induced strengthening. a Dislocations in the sample solutioned at 450°C/20 min and peak aging after tensile. **b** KAM mapping of the tensile fracture of the sample. **c** Crack propagation path of the sample during three-point bending testing. **d** Loading-Unloading-Reloading (LUR) curves. **e** The third hysteresis loop of (**d**), in which σ_r and σ_u were defined using 5% slope reduction of Young's modulus. **f** HDI stress and the ratio of HDI stress to flow stress derived from the LUR hysteresis loops.

There is a larger loop area for the sample solutioned at 450°C/20 min and peak aging, indicating the bimodal grains promote the HDI stress. The HDI stress can be calculated as follows[18,44,45]:

$$\sigma_{HDI} = (\sigma_r + \sigma_u)/2 \tag{1}$$

where σ_{HDI} is the HDI stress, σ_r is the reloading yield stress, σ_u is the unloading yield stress. As shown in Fig. 5f, HDI stress and HDI stress/flow stress ratio gradually increase with the increase of true strain, implying that the alloy has obvious work hardening and strength uplift. As shown in Fig. 2d, it can be inferred that the contribution of HDI to yield strength in the samples treated with 450°C/20 min solid solution and peak aging is ~10%. It has been reported that an appropriate strain distribution can be achieved by adjusting the volume fraction of the coarse/fine region and the grain size distribution, which enables tunable mechanical properties[51,52]. In this work, the ratio of CGs/FGs can be adjusted by changing the printing parameters, the number of nucleant particles and the post-heat treatment parameters, thus the desired strength/ductility matching can be achieved.

Figure 5c shows a crack propagation path of the sample during three-point bending testing, demonstrating an intergranular crack mode in the FGs zone and a transgranular one in the CGs zone. During tensile deformation, micropores initially form at the weak grain boundaries with the coarse phases and then aggregate into microcracks[53,54]. Therefore, cracks can nucleate and propagate quickly through the FGs zone, but will be blunted and slowed down when they encounter ductile CGs. In addition, the excellent dislocation storage capacity of CGs helps facilitate work hardening and thereby enhances the ductility[42,45,49,55].

Conclusions

In summary, the as-built heterostructure produced in solidified molten pools, including alternating Fine Grains (FGs) and Ultrafine Grains (UFGs) zones with nonuniformly distributed primary Al$_3$Nb particles, dislocations and residual stress, provides different driving forces and Zener pinning sources for recrystallization to create a bimodal grain structure after solution treatment. The bimodal grain structure provides an additional strengthen mechanism in the alloys: HDI strengthening and HDI work hardening. Along with excellent precipitation hardening from the high number density of η′ nanoprecipitates, the improved strength and ductility were achieved. The strategy we have proposed here is easily implemented with associated cost savings, and is also applicable to other heat-treated alloys, such as copper alloys, titanium alloys, magnesium alloys, nickel-based superalloys and steel, processed via various AM technologies, such as LPBF, direct energy deposition and electron-beam melting.

Methods

Powders preparation

Al-11Zn-2.4Mg-1.6Cu (in wt.%, if not stated otherwise) ingots with other trace elements (0.034%Ti, 0.322%Fe, 0.054%Si, 0.215%Cr) were prepared in an electric resistance furnace using pure Al, pure Zn, pure Mg and Al-50Cu master alloy. Then, the spherical powders were prepared by Ar gas-atomization (Nantong Jinyuan Intelligent Co., Ltd). Spherical pure Nb (99.9% purity) nanoparticles with an average size of ~50 nm were commercially purchased from Chaowei Nano Co., Ltd. Aluminum alloy powders and 1.5% Nb nanoparticles were mixed for 2 h in a TURBULA T2F planetary shaker-mixer. Figure 6a displays that the morphology of the Nb nanoparticles-modified Al-Zn-Mg-Cu powders. As shown in the yellow box of Figs. 6b and 6c, Nb nanoparticles are evenly distributed on the surface of aluminum alloy powders. As shown in Fig. 6d, the size of the aluminum alloy powders is approximately normal distribution with average particle size is ~45 μm (D10 = 23 μm, D50 = 42 μm, D90 = 78 μm). Figure 6e presents that the sphericity of most powders is more than 90%, implying that the powder has good fluidity.

Laser powder bed fusion

The LPBF experiments were performed on a 3D printing machine (SLM Solutions, SLM125HL) equipped with a maximum laser power of 400 W.
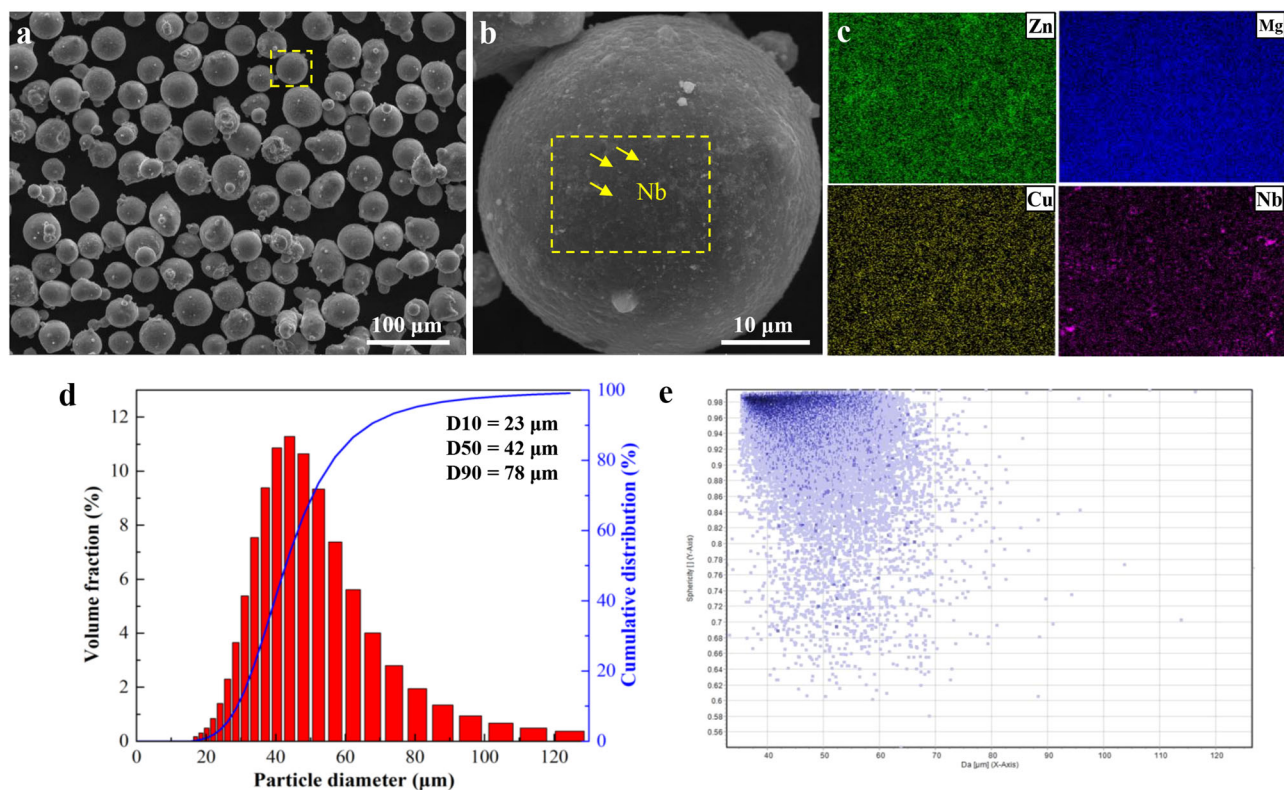
Fig. 6 | Characterization of Powders. a Morphology of the Nb nanoparticles-modified Al-Zn-Mg-Cu alloy powders. **b** Surface morphology of the powder in the yellow box of (**a**). **c** Element mapping of the surface in (**b**). **d** Size distribution of the Al-Zn-Mg-Cu alloy powders. **e** sphericity of the powders.

The laser with a wavelength of 1070 nm and a spot diameter of 79 μm had a Gaussian power profile. A relatively large Ar gas flow was used to continuously purge the printing chamber to reduce the harmful effect of splash caused by the evaporation of low melting point elements Zn and Mg. The oxygen content was <100 ppm, and the preheating temperature of the 7075 substrate was ~150 °C. As shown in Supplementary Fig. 12, the printing strategy with an interlayer rotation angle of 67°. The as-built samples without obvious cracks were obtained using the optimized process parameters (laser power 175 W, scanning speed 600 mm/min, layer thickness 30 μm, and hatching space 0.12 mm), and its relative density measured by Archimedes method is ~99.7%. Owing to the high vapor pressure of Zn and Mg elements and the instantaneous high temperature of the laser, Zn and Mg were inevitably burnt off during LPBF, resulting in the actual alloy composition as Al-9.5Zn-2.2Mg-1.6Cu-1.5 Nb.

Post heat treatment
The post heat treatment process included solid solution and peak aging. The samples were heated to 450–490 °C at a rate of 10 °C/min for 0-120 min, and then water quenched, which are the frequently used solution parameters for Al-Zn-Mg-Cu alloys. In order to obtain the highest number density of nanoprecipitates, peak aging (120 °C/24 h) was performed in an oil bath furnace.

Microstructure characterization
The microstructure of as-built samples and post heat treated samples were observed using an optical microscope (OM, OLYMPUS) and a scanning electron microscope (SEM, TESCAN Mira 3) equipped with an energy-dispersive spectroscopy (EDS). Samples were etched with a 5 vol.% HF solution. The bimodal structures were characterized by electron backscatter diffraction (EBSD, TESCAN GAIA 3), and then the grain size distribution and coarse/fine grain volume fraction were measured using a Channel 5 Software and an ImageJ Software. In order to facilitate the statistical analysis of the size of irregularly shaped grains, the equivalent circle method was

adopted. Samples for EBSD analysis were prepared by mechanical polishing combined with ion beam surface cutting to remove the surface residual stress. Bright field (BF) images of precipitates and dislocations were obtained using a transmission electron microscope (TEM, FEI Talos F200X G2). High resolution TEM (HRTEM) images of precipitates were observed under the [011] axis of the α-Al matrix. The samples used for TEM were first mechanically ground to 80 μm and cut into φ3 mm discs, and then were electrochemically thinned in a 25 vol.% nitric acid methanol solution with the temperature of −30°C and the voltage of ~50 V.

In order to investigate the evolution of the bimodal microstructure during heat treatment, a quasi in-situ EBSD experiment was carried out. First, the as-built sample for EBSD characterization was prepared by mechanical polishing combined with ion beam surface cutting. Then, an area with a size of 1000 × 1000 μm was encircled by a series of hardness indentations on the surface of the as-built sample, and the evenly distributed hardness indentations were used as reference coordinates for accurate positioning. The size of the characterization area includes at least one solidified molten pool and its position was recorded. After EBSD characterization of the as-built sample, it was enclosed in a quartz tube and heat treated under an Ar atmosphere to prevent oxidation. The quasi in-situ EBSD observation of the heat-treated sample was then performed on the same area. The experimental data of the quasi in-situ EBSD were analyzed using channel 5 software.

Microhardness testing
Vickers hardness testing was carried out in the CGs and FGs zones respectively to characterize the difference in mechanical properties of the bimodal microstructure on a microhardness test machine (402 SXV) with a load of 20 g and a dwell time of 15 s.

Tensile properties testing
A tensile testing machine (Zwick/Roell Z100) with a strain rate of 1×10^{-3} s^{-1} was used to test tensile properties at room temperature. To ensure reliability

     Article

of data, three samples in each state were prepared and the average value of the tensile properties were calculated.

Three-point bending test

A three-point bending experiment at room temperature was conducted to investigate the influence of bimodal grain structure on crack propagation during fracture. Before the three-point bending experiment, a single edge cut was prefabricated using wire cutting. The experiment was conducted on a testing machine (Zwick/Roell Z100) with a strain rate of 0.2 mm/min and a span of 25 mm. In order to preserve the deflection path and morphology changes of the cracks, the test was stopped before the specimen was crushed.

Loading-unloading-reloading tensile testing

To calculate the HDI stress, loading-unloading-reloading tensile tests were carried out at room temperature with a strain rate of 1×10^{-3} s^{-1} on a testing machine (Instron 5565). The unloading strain rate is the same as the loading strain rate.

Data availability

All datasets generated and analyzed throughout this work are available from the corresponding author upon reasonable request.

References

1. Galy, C., Le Guen, E., Lacoste, E. & Arvieu, C. Main defects observed in aluminum alloy parts produced by SLM: from causes to consequences. *Addit. Manuf.* **22**, 165–175 (2018).
2. Gault, B. et al. Hot cracking mechanism affecting a non-weldable Ni-based superalloy produced by selective electron beam melting. *Acta Mater.* **142**, 82–94 (2018).
3. Martin, J. H. et al. 3D printing of high-strength aluminium alloys. *Nature* **549**, 365–369 (2017).
4. Lu, J. et al. On the Sc induced solidification-heterogeneous microstructure in selective laser melted Al-5Mn alloys. *J. Mater. Process Technol.* **304**, 117562 (2022).
5. Zhu, Z. et al. Superior mechanical properties of a selective-laser-melted AlZnMgCuScZr alloy enabled by a tunable hierarchical microstructure and dual-nanoprecipitation. *Mater. Today* **52**, 90–101 (2022).
6. Wang, T., Wang, Y., Yang, X., Chen, B. & Zhu, H. Cracks and process control in laser powder bed fusion of Al-Zn-Mg alloy. *J. Manuf. Process* **81**, 571–579 (2022).
7. Stopyra, W., Gruber, K., Smolina, I., Kurzynowski, T. & Kuźnicka, B. Laser powder bed fusion of AA7075 alloy: influence of process parameters on porosity and hot cracking. *Addit. Manuf.* **35**, 101270 (2020).
8. Zhou, S. Y. et al. Selective laser melting additive manufacturing of 7xxx series Al-Zn-Mg-Cu alloy: cracking elimination by co-incorporation of Si and TiB2. *Addit. Manuf.* **36**, 101458 (2020).
9. Zhang, J. et al. A novel crack-free Ti-modified Al-Cu-Mg alloy designed for selective laser melting. *Addit. Manuf.* **38**, 101829 (2021).
10. Xiao, F. et al. Effect of Zn content on the formability and aging precipitation of Al-Zn-Mg-Cu-Nb alloys prepared by LPBF. *J. Mater. Res. Technol.* **25**, 6338–6355 (2023).
11. Babu, A. P., Kairy, S. K., Huang, A. & Birbilis, N. Laser powder bed fusion of high solute Al-Zn-Mg alloys: processing, characterisation and properties. *Mater. Des.* **196**, 109183 (2020).
12. Babu, A. P., Huang, A. & Birbilis, N. On the heat treatment and mechanical properties of a high solute Al-Zn-Mg alloy processed through laser powder bed fusion process. *Mater. Sci. Eng. A* **807**, 140857 (2021).
13. Wu, S., Lei, Z., Li, B., Liang, J. & Chen, Y. Hot cracking evolution and formation mechanism in 2195 Al-Li alloy printed by laser powder bed fusion. *Addit. Manuf.* **54**, 102762 (2022).
14. Chen, H., Zhang, Y., Giam, A. & Yan, W. Experimental and computational study on thermal and fluid behaviours of powder layer during selective laser melting additive manufacturing. *Addit. Manuf.* **52**, 102645 (2022).
15. Li, J. et al. Simultaneously enhanced strength and ductility of Cu-15Ni-8Sn alloy with periodic heterogeneous microstructures fabricated by laser powder bed fusion. *Addit. Manuf.* **54**, 102726 (2022).
16. Wu, S. W. et al. Enhancement of strength-ductility trade-off in a high-entropy alloy through a heterogeneous structure. *Acta Mater.* **165**, 444–458 (2019).
17. Witkin, D., Lee, Z., Rodriguez, R., Nutt, S. & Lavernia, E. Al-Mg alloy engineered with bimodal grain size for high strength and increased ductility. *Scr. Mater.* **49**, 297–302 (2003).
18. Kong, D. et al. Hetero-deformation-induced stress in additively manufactured 316L stainless steel. *Mater. Res. Lett.* **8**, 390–397 (2020).
19. Wang, M., Song, B., Wei, Q., Zhang, Y. & Shi, Y. Effects of annealing on the microstructure and mechanical properties of selective laser melted AlSi7Mg alloy. *Mater. Sci. Eng. A* **739**, 463–472 (2019).
20. Wu, X. et al. Heterogeneous lamella structure unites ultrafine-grain strength with coarse-grain ductility. *Proc. Natl Acad. Sci. USA* **112**, 14501–14505 (2015).
21. Wang, Y., Chen, M., Zhou, F. & Ma, E. High tensile ductility in a nanostructured metal. *Nature* **419**, 549 (2002).
22. Xiao, F. et al. Niobium nanoparticle-enabled grain refinement of a crack-free high strength Al-Zn-Mg-Cu alloy manufactured by selective laser melting. *J. Alloy. Compd.* **900**, 163427 (2022).
23. Ma, K. et al. Mechanical behavior and strengthening mechanisms in ultrafine grain precipitation-strengthened aluminum alloy. *Acta Mater.* **62**, 141–155 (2014).
24. Zhao, S., Meng, C., Mao, F., Hu, W. & Gottstein, G. Influence of severe plastic deformation on dynamic strain aging of ultrafine grained Al-Mg alloys. *Acta Mater.* **76**, 54–67 (2014).
25. Wang, Z. et al. Strength-ductility synergy of selective laser melted Al-Mg-Sc-Zr alloy with a heterogeneous grain structure. *Addit. Manuf.* **34**, 101260 (2020).
26. Wang, Z. et al. Laser powder bed fusion of high-strength Sc/Zr-modified Al-Mg alloy: phase selection, microstructural/mechanical heterogeneity, and tensile deformation behavior. *J. Mater. Sci. Technol.* **95**, 40–56 (2021).
27. Martin, J. H. et al. Grain refinement mechanisms in additively manufactured nano-functionalized aluminum. *Acta Mater.* **200**, 1022–1037 (2020).
28. Wang, Y. et al. Laser powder bed fusion of Zr-modified Al–Cu–Mg alloy: crack-inhibiting, grain refinement, and mechanical properties. *Mater. Sci. Eng. A* **838**, 142618 (2022).
29. Wang, Z. et al. Directed energy deposition additive manufacturing of a Sc/Zr-modified Al–Mg alloy: effect of thermal history on microstructural evolution and mechanical properties. *Mater. Sci. Eng. A* **802**, 140606 (2021).
30. Li, Q. et al. Development of a high strength Zr/Sc/Hf-modified Al-Mn-Mg alloy using laser powder bed fusion: design of a heterogeneous microstructure incorporating synergistic multiple strengthening mechanisms. *Addit. Manuf.* **57**, 102967 (2022).
31. Adam, K. F., Long, Z. & Field, D. P. Analysis of particle-stimulated nucleation (PSN)-dominated recrystallization for hot-rolled 7050 aluminum alloy. *Met. Mater. Trans. A Phys. Met. Mater. Sci.* **48**, 2062–2076 (2017).
32. She, H. et al. Relationship of particle stimulated nucleation, recrystallization and mechanical properties responding to Fe and Si contents in hot-extruded 7055 aluminum alloys. *J. Mater. Sci. Technol.* **35**, 2570–2581 (2019).
33. Knipling, K. E., Dunand, D. C. & Seidman, D. N. Criteria for developing castable, creep-resistant aluminum-based alloys - a review. *Int J. Mater. Res.* **97**, 246–265 (2006).

34. Chen, L., Wang, H., An, X. & Huang, X. Recovery, recrystallization and precipitation behavior in an ATF FeCrAl alloy during annealing treatment. *Mater. Charact.* **190**, 112026 (2022).

35. Fu, X. et al. Enhanced strain hardening by bimodal grain structure in carbon nanotube reinforced Al–Mg composites. *Mater. Sci. Eng. A* **803**, 140726 (2021).

36. Wang, Y. & Shi, J. Effect of hot isostatic pressing on nanoparticles reinforced AlSi10Mg produced by selective laser melting. *Mater. Sci. Eng. A* **788**, 139570 (2020).

37. Zou, Y. et al. Investigation on microstructure and mechanical properties of Al-Zn-Mg-Cu alloys with various Zn/Mg ratios. *J. Mater. Sci. Technol.* **85**, 106–117 (2021).

38. Hall, E. O. The deformation and ageing of mild steel: III discussion of results. *Proc. Phys. Soc. Sect. B* **64**, 747–753 (1951).

39. Zhu, Y. & Wu, X. Heterostructured materials. *Prog. Mater. Sci.* **131**, 101019 (2023).

40. Ma, X. L. et al. Strain hardening and ductility in a coarse-grain/nanostructure laminate material. *Scr. Mater.* **103**, 57–60 (2015).

41. Brandstetter, S. et al. From micro- to macroplasticity. *Adv. Mater.* **18**, 1545–1548 (2006).

42. Ma, E. & Zhu, T. Towards strength–ductility synergy through the design of heterogeneous nanostructures in metals. *Mater. Today* **20**, 323–331 (2017).

43. Ashby, M. F. The deformation of plastically non-homogeneous materials. *Philos. Mag.* **21**, 399–424 (1970).

44. Chen, X. et al. Design of pure aluminum laminates with heterostructures for extraordinary strength-ductility synergy. *J. Mater. Sci. Technol.* **100**, 193–205 (2022).

45. Zhang, C. L. et al. Achieving superior strength-ductility balance in a novel heterostructured strong metastable β-Ti alloy. *Int J. Plast.* **147**, 103126 (2021).

46. Chen, X., Zhang, B., Zou, Q., Huang, G. & Liu, S. Journal of materials science & technology design of pure aluminum laminates with heterostructures for extraordinary strength-ductility synergy. *J. Mater. Sci. Technol.* **100**, 193–205 (2022).

47. Mohammed, S. M. A. K. et al. Deformation behavior and strengthening mechanisms in a CNT-reinforced bimodal-grained aluminum matrix nanocomposite. *Mater. Sci. Eng.* **817**, 141370 (2021) .

48. Yang, M., Pan, Y., Yuan, F., Zhu, Y. & Wu, X. Back stress strengthening and strain hardening in gradient structure. *Mater. Res. Lett.* **4**, 145–151 (2016).

49. Zhu, Y. et al. Heterostructured materials: superior properties from hetero-zone interaction. *Mater. Res. Lett.* **9**, 1–31 (2021).

50. Zhu, Y. & Wu, X. Perspective on hetero-deformation induced (HDI) hardening and back stress. *Mater. Res. Lett.* **7**, 393–398 (2019).

51. Shin, S., Zhu, C., Zhang, C. & Vecchio, K. S. Extraordinary strength-ductility synergy in a heterogeneous-structured β -Ti alloy through microstructural optimization. *Mater. Res Lett.* **7**, 467–473 (2019).

52. Zhu, J. et al. Real time observation of equiaxed growth of Sn-Pb alloy under an applied direct current by synchrotron microradiography. *Mater. Lett.* **89**, 137–139 (2012).

53. Luo, X. et al. Evading strength and ductility trade-off in an inverse nacre structured magnesium matrix nanocomposite. *Acta Mater.* **228**, 117730 (2022).

54. Zok, F. W. & Spearing, S. M. Matrix crack spacing in brittle matrix composites. *Acta Met. Mater.* **40**, 2033–2043 (1992).

55. Fu, Y. et al. Ultrahigh strain hardening in a transformation-induced plasticity and twinning-induced plasticity titanium alloy. *Scr. Mater.* **187**, 285–290 (2020).

56. Wang, P. et al. Microstructure and mechanical properties of a heat-treatable Al-3.5Cu-1.5Mg-1Si alloy produced by selective laser melting. *Mater. Sci. Eng. A* **711**, 562–570 (2018).

57. Michi, R. A. et al. Microstructural evolution and strengthening mechanisms in a heat-treated additively manufactured Al-Cu-Mn-Zr alloy. *Mater. Sci. Eng. A* **840**, 142928 (2022).

58. Wang, Y. et al. Influence of post-heat treatment on the microstructure and mechanical properties of Al-Cu-Mg-Zr alloy manufactured by selective laser melting. *J. Mater. Sci. Technol.* **111**, 35–48 (2022).

59. Li, G. et al. Exploiting the rapid solidification potential of laser powder bed fusion in high strength and crack-free Al-Cu-Mg-Mn-Zr alloys. *Addit. Manuf.* **47**, 102210 (2021).

60. Zhao, J. et al. Study of in situ formed quasicrystals in Al-Mn based alloys fabricated by SLM. *J. Alloy. Compd.* **909**, 164847 (2022).

61. Jia, Q., Rometsch, P., Kürnsteiner, P., Chao, Q. & Huang, A. Selective laser melting of a high strength Al-Mn-Sc alloy: alloy design and strengthening mechanisms. *Acta Mater.* **171**, 108–118 (2019).

62. Wei, P. et al. Microstructure and mechanical properties of graphene and nano-zirconia reinforced AlSi10Mg composite fabricated by laser powder bed fusion. *Mater. Sci. Eng. A* **864**, 144574 (2023).

63. Xiao, Y. K. et al. Enhancing strength and ductility of AlSi10Mg fabricated by selective laser melting by TiB2 nanoparticles. *J. Mater. Sci. Technol.* **109**, 254–266 (2022).

64. Jiang, L. Y. et al. Preparation and mechanical properties of CNTs-AlSi10Mg composite fabricated via selective laser melting. *Mater. Sci. Eng. A* **734**, 171–177 (2018).

65. Xiao, Y. K. et al. Microstructure, heat treatment and mechanical properties of TiB2/Al-7Si-Cu-Mg alloy fabricated by selective laser melting. *Mater. Sci. Eng. A* **809**, 140951 (2021).

66. He, P. et al. Fatigue and dynamic aging behavior of a high strength Al-5024 alloy fabricated by laser powder bed fusion additive manufacturing. *Acta Mater.* **220**, 117312 (2021).

67. Zhou, L. et al. Microstructure and mechanical properties of Zr-modified aluminum alloy 5083 manufactured by laser powder bed fusion. *Addit. Manuf.* **28**, 485–496 (2019).

68. Bi, J. et al. Densification, microstructure and mechanical properties of an Al-14.1Mg-0.47Si-0.31Sc-0.17Zr alloy printed by selective laser melting. *Mater. Sci. Eng. A* **774**, 138931 (2024).

69. Mehta, A. et al. Additive manufacturing and mechanical properties of the dense and crack free Zr-modified aluminum alloy 6061 fabricated by the laser-powder bed fusion. *Addit. Manuf.* **41**, 101966 (2021).

70. Zhou, L. et al. Microstructure and tensile property of a novel AlZnMgScZr alloy additively manufactured by gas atomization and laser powder bed fusion. *Scr. Mater.* **158**, 24–28 (2019).

71. Tan, Q. et al. A novel strategy to additively manufacture 7075 aluminium alloy with selective laser melting. *Mater. Sci. Eng. A* **821**, 141638 (2021).

72. Otani, Y. & Sasaki, S. Effects of the addition of silicon to 7075 aluminum alloy on microstructure, mechanical properties, and selective laser melting processability. *Mater. Sci. Eng. A* **777**, 139079 (2020).

73. Gao, R., Li, Y., Li, Z. & Li, X. Quantitative relationship between microstructure and tensile properties of Al-Zn-Mg-Cu alloys with various alloying degrees. *J. Mater. Res Technol.* **18**, 5394–5405 (2022).

74. Li, L. et al. Microstructures and tensile properties of a selective laser melted Al-Zn-Mg-Cu (Al7075) alloy by Si and Zr microalloying. *Mater. Sci. Eng. A* **787**, 139492 (2020).

75. Li, X., Li, G., Zhang, M. & Zhu, Q. Novel approach to additively manufacture high-strength Al alloys by laser powder bed fusion through addition of hybrid grain refiners. *Addit. Manuf.* **48**, 102400 (2021).

76. Li, X., Li, D., Li, G. & Cai, Q. Microstructure, mechanical properties, aging behavior, and corrosion resistance of a laser powder bed fusion fabricated Al–Zn–Mg–Cu–Ta alloy. *Mater. Sci. Eng. A* **832**, 142364 (2022).

Acknowledgements

Competing interests

The authors declare no competing interests.

Additional information

Supplementary information The online version contains supplementary material available at https://doi.org/10.1038/s43246-024-00489-1.

Correspondence and requests for materials should be addressed to Da Shu or Baode Sun.

Reprints and permissions information is available at http://www.nature.com/reprints

Publisher's note Springer Nature remains neutral with regard to jurisdictional claims in published maps and institutional affiliations.